

# Effects of Local Wall Heating and Cooling on Hypersonic Boundary-Layer Stability

By P. Polivanov<sup>†</sup>, Y. Gromyko<sup>†</sup>, A. Sidorenko<sup>†</sup>, A. Maslov<sup>†</sup>,  
M. Keller<sup>‡</sup>, G. Groskopf<sup>‡</sup> AND M. J. Kloker<sup>‡</sup>

<sup>†</sup>Khrstianovich Institute of Theoretical and Applied Mechanics (ITAM)  
Russia 630090, Novosibirsk, Institutskaya str., 4/1

<sup>‡</sup>Institut für Aerodynamik und Gasdynamik, Universität Stuttgart  
Pfaffenwaldring 21, 70569 Stuttgart, Germany

The paper presents the stability analysis of a hypersonic boundary layer, perturbed by a local heating/cooling element at the wall. The study is performed for a freestream Mach number and a unit Reynolds number of  $M_\infty = 5.4$  and  $Re_{unit} = 4.8 \cdot 10^6 1/m$ , respectively. At first, simulations are carried out for a two-dimensional control element with different temperatures and lengths at various positions. The results obtained by direct numerical simulations for 2-d disturbances are in good agreement with linear stability theory. It is shown that local wall heating increases the disturbance amplitude in downstream direction, however, in the heated zone perturbations are stabilized. In case of cooling, the opposite effect was discovered, namely a significant increase of the disturbance magnitude on the element and damping downstream. Furthermore, three-dimensional effects of a cooling/heating element with finite extent in spanwise direction are considered. Bi-global linear stability theory in flow crosscuts is employed to investigate the stability behavior of the thermally perturbed hypersonic boundary-layer flow. It is shown that despite the three-dimensionality of the thermal element 1<sup>st</sup>-mode disturbances still play a minor role. For the investigated setup 3-d effects are found to be rather weak and apparently are limited to the region of the element.

---

## 1. Introduction

The development of secure and re-usable re-entry vehicles requires the complete control of the heat distribution on its Thermal Protection System (TPS). During the most critical re-entry phase, the hypersonic flow along the vehicle initiates a laminar boundary layer inside of which most of the transfer phenomena take place (heat, momentum and mass transfer). If at one position of the vehicle, this boundary layer experiences a transition from the laminar to the turbulent regime the TPS will receive a sharp increase of the incoming heat flux (minimum 3 times higher at the corresponding position). For re-usability it is mandatory to protect the vehicle adequately against this overheat. Therefore, aerospace designers need to receive the proper information and tools allowing for a better prediction and ultimately a better control of the transition in the hypersonic regime.

For aerospace engineers the design of new hypersonic vehicles requires accurately predicted and effectively controlled heat loads on its TPS in order to avoid a destructive accident during the re-entry in the atmosphere. The lack of reliable methods obliges vehicle designers to use a conservative approach and, thus, to oversize the thermal

protection system. As a consequence, the part of total mass budget dedicated to the payload is reduced to a few percent.

For configurations having aerodynamically smooth surfaces, transition is associated with excitation in the boundary layer and downstream amplification of unstable modes, namely, the first and second modes. Although features of these instabilities and opportunities of their control have been studied by the research community for more than fifty years, they have been focused on boundary layers having fairly uniform distributions of the wall temperature and heat flux.

However, actual TPS may have elements of different heat conductivity and/or emissivity. Junctures between these elements lead to jumps of the heat-transfer boundary conditions. Furthermore, active TPS may produce regions of localized relative heating or cooling of the aerodynamic surface. These thermal non-uniformities may significantly affect the boundary-layer mean flow, excitation and evolution of unstable modes and, ultimately, the transition locus. The investigation of the physical mechanisms associated with the foregoing thermal effects will help us to design advanced thermal protection systems providing capabilities of transition control.

The localized surface heating has been already experienced in ground facility but only up to the supersonic regime. Recently, DNS studies of Soudakov *et al.* [1] of flow disturbances interacting with the wall-temperature jumps on a flat plate in a Mach 6 free stream flow were carried out. It was found that these jumps affect both stability and receptivity of the boundary layer.

The remainder of this paper is organized as follows: Section 2 describes the analysis of the two-dimensional heating/cooling element for various temperatures, lengths and positions. The effects of a three-dimensional element on the flow stability are presented in Sec. 3. Finally, Sec. 4 summarizes the main findings and contains some concluding remarks.

## 2. Two-dimensional simulations

### 2.1. Problem formulation

An effect of the local cooling/heating on the development of the boundary layer disturbances was studied numerically for the test case of the hypersonic flow formulated above for the flat plate under zero angle of attack (Fig. 1). It is well known that in this case the transition is determined by development of the most unstable second mode. It was also shown that the most amplified disturbances of the second mode have zero angle of incidence to the mean flow direction [2,3].

Numerical simulation of the disturbances development in the boundary layer was carried out using the linear stability theory (LST) and direct numerical simulation (DNS). Taking into account the above mentioned consideration, DNS simulation was performed for 2-d first and second mode disturbances. The Commercial CFD software Fluent 6.3 was used. LST was used for the study of the influence of local cooling / heating on the evolution of the first-mode perturbations (which is most unstable for nonzero angle of incidence).

All calculations were carried out for flat plate model of 300 mm length for the following free-stream parameters:  $M_\infty = 5.4$ ,  $P_\infty = 389 Pa$ ,  $T_\infty = 59 K$ . The preliminary estimations revealed that the effects of numerical viscosity in DNS may be neglected if grid has at least 50 cells per wavelength of the disturbance. Therefore the computational grid consisted of  $3100 \times 137$  cells and corresponded to physical domain of  $310 \times 45 mm$ . The

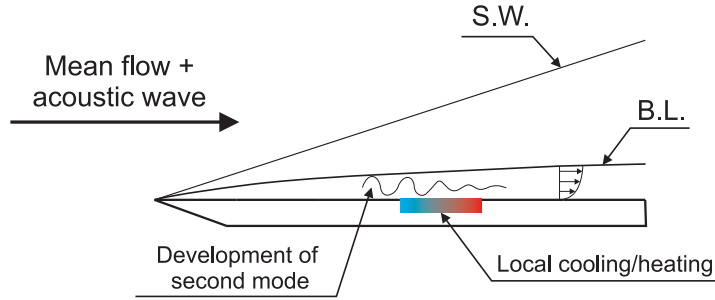


FIGURE 1. Problem formulation.

grid was uniform in streamwise and normal to the wall directions in the boundary layer (80 cells) and rarefied to the upper boundary. This kind of grid allowed to calculate the development of disturbances with frequency up to 170 kHz. Generation of disturbances was carried out by specifying the input boundary conditions for the propagation of slow acoustic wave:

$$P = P_{\infty} + P' = P_{\infty} + \epsilon \cdot \sin(\omega t + \varphi) \cdot \rho_{\infty} u_{\infty}^2 \quad (2.1)$$

$$T = T_{\infty} + T' = T_{\infty} + \epsilon \cdot \sin(\omega t + \varphi) \cdot (\gamma - 1) \cdot M_{\infty}^2 \cdot T_{\infty} \quad (2.2)$$

$$M = u/a, \quad u = u_{\infty} + u' = u_{\infty} - u_{\infty} \cdot M_{\infty} \cdot \epsilon \cdot \sin(\omega t + \varphi) \quad (2.3)$$

$$a = a_{\infty} + a' = \sqrt{\gamma \cdot R \cdot (T_{\infty} + T')} \quad (2.4)$$

Here, the subscript  $\infty$  corresponds to steady freestream parameters, the index ' corresponds to the fluctuating component (acoustic wave), and parameter  $\epsilon$  is a dimensionless amplitude of the disturbances.

Sequential analysis of many frequencies is not efficient because the growth of perturbations occurs in a wide range of frequencies. A separate review of a large number of discrete frequencies requires a substantial amount of computation time. Therefore it was decided to use the linear combination of several harmonic waves of equal amplitude as the initial perturbation. This combination included 13 waves of frequencies from 55 to 175 kHz with increment of 10 kHz. The preliminary calculations have shown a good agreement between the level of perturbation obtained in batch mode and reconstructed as sum of the individual frequencies.

It is clear that 2D formulation of the problem can not reliably assess the development of nonlinear processes. To consider only the linear stage of the disturbance development it was necessary to choose correctly the amplitude of initial perturbations. In the preliminary calculations it was found that this value must not exceed  $\epsilon = 0.5e^{-5}$ .

The steady distributions of the flow parameters across the boundary layer obtained in DNS were used as local profiles for LST analysis. For every test case 105 local profiles were calculated distributed from  $x = 40 \text{ mm}$  to  $x = 300 \text{ mm}$  with increment of  $2.5 \text{ mm}$ . The preliminary estimations revealed that the maximum amplification of the first mode disturbances corresponds to  $\chi = 55^\circ$ . It allowed us to save the CPU time and consider only wave inclination angles of  $\chi = 0^\circ$  and  $\chi = 55^\circ$  corresponding to the first and second modes of disturbances.

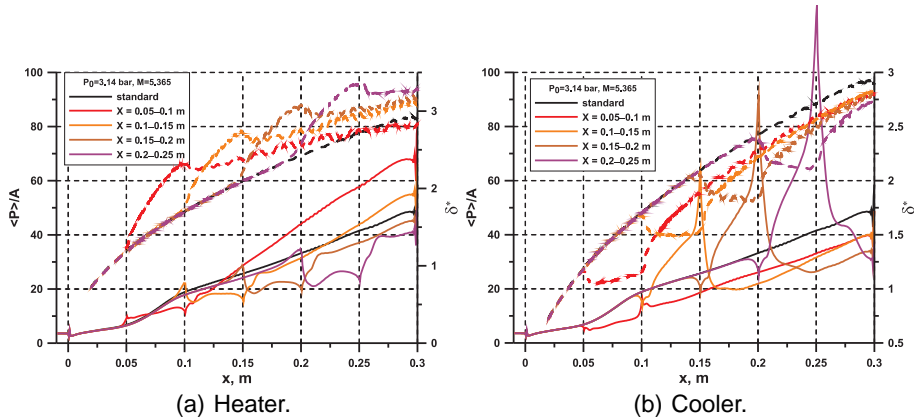


FIGURE 2. Distributions of pressure fluctuations on the wall and  $\delta^*$  for the various locations of the control element.

## 2.2. DNS results

The simulation of the boundary layer disturbance development with local heating and cooling of the wall was carried out for the wall temperature  $T_W = 290 \text{ K}$ . The temperature, location and extension of the cooler/heater region were varied.

Figure 2(a) and Fig. 2(b) show the RMS amplitude of pressure pulsations on the wall  $\langle P_W \rangle$  and displacement thickness  $\delta^*$  along the wall for the several cases: reference (base) as well as corresponding to heating and cooling of the wall at various locations ( $0.05 - 0.1 \text{ m}$ ,  $0.1 - 0.15 \text{ m}$ ,  $0.15 - 0.2 \text{ m}$ ,  $0.2 - 0.25 \text{ m}$ ). It can be seen from Fig.2 that the wave packet begins to grow rapidly from  $x = 0.07 \text{ m}$ . In the base case there is monotonic increase of RMS value of the pulsations downstream.

It can be seen from the Fig. 2(a), that immediately downstream of the heater there is damping of the perturbations amplitude, but after that level of pulsations begins to grow and becomes greater than base value. This result was obtained for the heater located of at  $x = 0.05 - 0.1 \text{ m}$  and  $0.1 - 0.15 \text{ m}$ . It is obvious that with increasing length of the computational domain the same behavior of disturbances may be obtained for the heater placed at  $x = 0.15 - 0.2 \text{ m}$  and  $0.2 - 0.25 \text{ m}$ .

Local cooling of the surface leads to more significant changes of the pulsations amplitude due to extreme amplification of one or several waves of the packet in the cooled zone. This effect is connected with almost constant boundary-layer thickness in this region and destabilizing effect of the wall cooling. Except of the extremely amplified waves the rest of waves are stabilized, which causes reducing of the packet amplitude downstream of the cooling zone.

From the Fig. 2(b) and the following figures it can be seen that there is a peak of disturbance magnitude at the end of the cooler. Such a behavior of pulsations was initially connected with possible BL receptivity processes to external acoustics. The receptivity may be caused by presence of the slow acoustic wave above the boundary layer and strong variation of the boundary-layer thickness in this region. To clarify this question an additional study was performed. In these computations the pulsations inside the boundary layer were excited by means of synthetic jet on the wall instead of external acoustics. The data obtained coincide with the data presented above so we may conclude that all features of the wave packet development near the cooler/heater are connected with boundary layer stability.

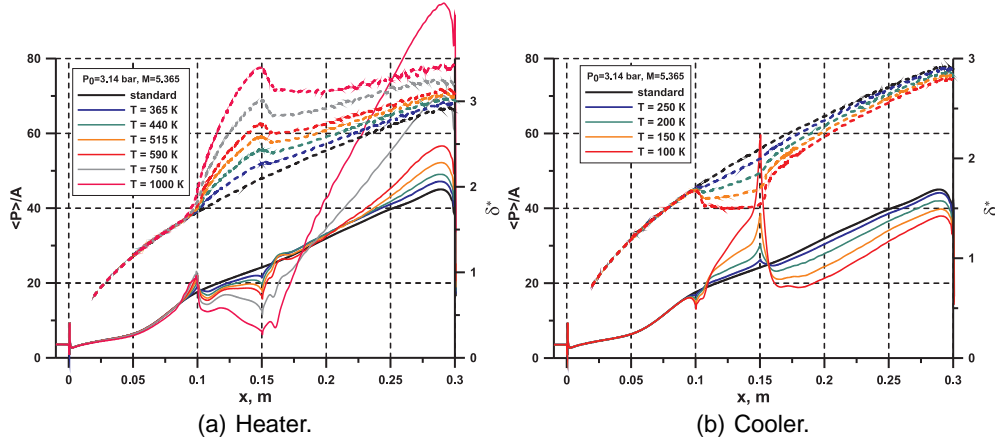


FIGURE 3. Distributions of  $\langle P \rangle$  and  $\delta^*$  for the various temperature of the control element.

Figure 3 shows  $\langle P_W \rangle$  and  $\delta^*$  distributions presented for various temperature of control element located at  $x = 0.1 - 0.15 m$ . The increase of its temperature  $T_c$  from 365 K to 1000 K is accompanied by gradual decrease of pulsation amplitude in the zone of heating. It is obvious that in this case there are two effects acting together: stabilization of the second mode due to increase of the wall temperature and detuning of the most amplified wave from the local BL parameters due to fast change of  $\delta$ . Downstream of the heater there is some amplification of the wave packet amplitude. This amplification may be dramatic for high  $T_c$  due to slow growth of  $\delta$ . In this case of almost parallel flow some waves are permanently amplified due to almost constant local parameters of the BL.

In the case of local cooling of the wall ( $T_c = 250K - 100K$ ) we can see that in the zone of control element there are favorable conditions for pulsation amplification. Besides the destabilization of the second mode (as it is known from LST) the wall cooling promotes conservation of the local BL parameters and amplification of the pulsations due to the tuning of several waves. The frequency range of these tuned waves are narrow therefore the most part of the waves are stabilized on the cooler and as a result the overall amplitude of the packet is decreased downstream of the control element. This effect is stronger for low  $T_c$ .

Figure 4 illustrates the effect of length of the control element  $L_c$  on the disturbances evolution. The wall distribution of pulsation amplitude and  $\delta^*$  are shown for several sizes of heater ( $T_c=100K$ ) and cooler ( $T_c=590K$ ). The control element starts from  $x = 0.1 m$  and extends for  $0.01 - 0.075 m$ . It is clear to see that the general behavior of pulsations corresponds to the data presented above. However the increase of the heater length does not result in strong pulsation decrease in this zone. Apparently it is connected with shape of the boundary layer above the heater. For the case of the cooler it can be seen that increasing of its length is favorable for destabilization of the wave packet. Additionally to cumulative effect of the cold wall on the second mode, the BL thickness in this case is constant allowing some waves to grow for a long time.

All the data presented show the existence of the sharp peaks in the wall pulsation distributions corresponded to the begin and the end of control element. The strongest peaks may be found at the end of the cooler and their strength marginally depends on

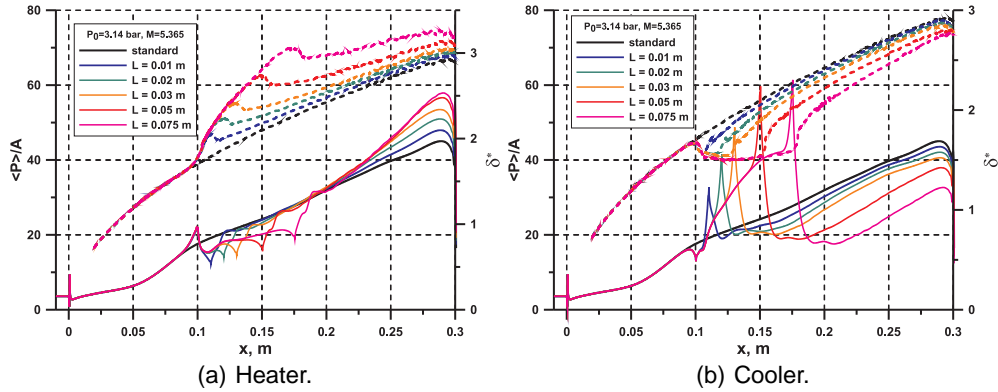


FIGURE 4. Distributions of  $\langle P \rangle$  and  $\delta^*$  for the various length of the control element.

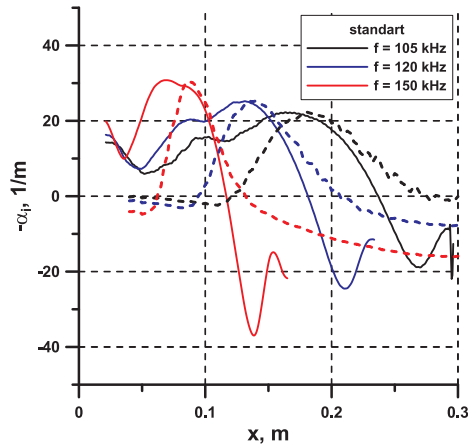


FIGURE 5. Comparison of the growth rates distribution along the plate (Solid - DNS, dashed - LST).

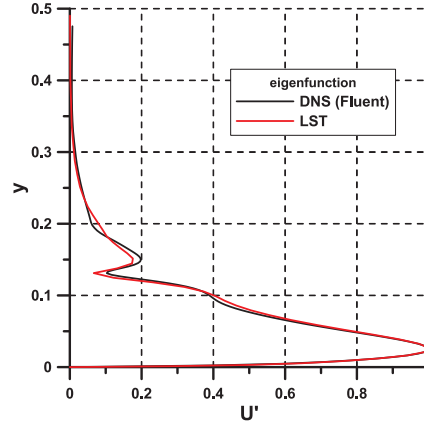


FIGURE 6. Comparison of the velocity eigenfunctions obtained in the cooling zone (Black curve - DNS, Red curve - LST).

$L_c$ . It may be concluded that existence of these peaks is produced by the strong angular displacement of streamlines and accompanying compression and extension waves.

### 2.3. Results of LST and comparison with DNS

The comparison of the amplification rate distributions along the wall obtained from LST and DNS for the reference test case is presented in Fig. 5. Good agreement may be found only in the regions of maximum growth rate for all frequencies. The level of growth rate upstream from the zone of maximum amplification estimated by LST is lower compared to DNS, because LST does not take into account non-parallel flow [4, 5]. It is necessary to note that upstream of the maximum amplification zone DNS simulation does not reveal any pulsation damping (negative  $-\alpha_i$ ) region. As result of this effect we may expect wider frequency range of amplification of the second mode disturbances for the real unparallel BL. Assumption of the flow parallelism in LST results in more serious disagreement in the case of the local heating/cooling. The comparison of the local  $-\alpha_i$  obtained by LST and DNS showed that LST data may be used only for qualitative estimations.

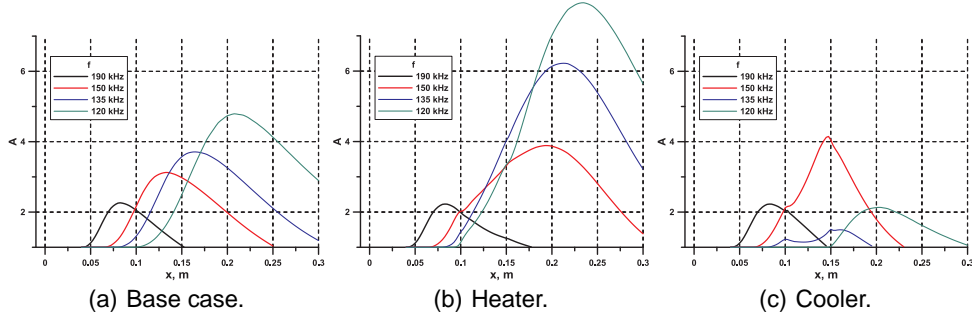


FIGURE 7. Distribution the amplitude of disturbances along the plate.

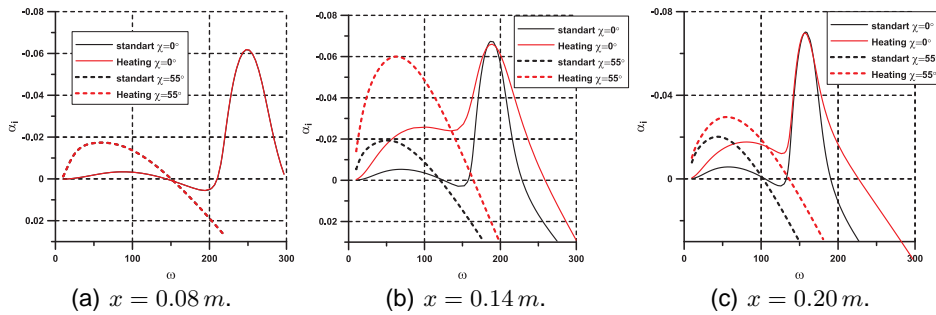


FIGURE 8. Spectra of growth rates (LST).

The comparison of velocity pulsation distributions across the BL calculated by LST and DNS codes near the cooling segment are presented in Fig. 6. There is good agreement of profiles, which means that perturbations in the both cases have the same nature (second mode).

Figure 7 shows the distributions of disturbance amplitude obtained by LST along the plate for various frequencies for  $\chi = 0^\circ$  (second mode). In the reference case (plot 7(a)) the peak of fluctuation increases gradually along the plate with decreasing of frequency. For the case of heater position  $x = 0.1 - 0.15$  m and  $T_c = 590$  K (plot 7(b)) there is amplification of disturbances for the frequencies 135 and 120 kHz. There is also decreased amplification rate for  $f = 150$  kHz in the region of the heated segment and resulting shift of the amplification maximum downstream. For the test case of the cooling ( $T_c = 100$  K) applied in the same position (plot 7(c)) the situation is opposite. The disturbances of  $f = 150$  kHz are amplified in the region of wall cooling where the disturbances of lower frequencies are damped. These data agree with DNS results and allow to conclude that wall heating and cooling effectively change the frequency range of the most amplified disturbances.

One of the useful LST applications is possibility of analysis of 3D wave development (in particular, the first mode) using the mean flow parameters obtained from 2D DNS. Such approach allows to save computation time required for analysis.

Figure 8 shows the growth rate spectra for the first ( $\chi = 55^\circ$ ) and second ( $\chi = 0^\circ$ ) modes obtained upstream, in the region of and downstream of the heating segment. The growth rate and frequency normalized by the following formula:  $\alpha_i = \alpha_i^*/\delta$ ,  $\omega = \omega^* \cdot \nu_e/U_e^2$  ( $U_e$  and  $\nu_e$  is velocity and kinetic viscosity at the edge of boundary layer). Upstream the heater growth rate of the first mode is significantly lower comparing to

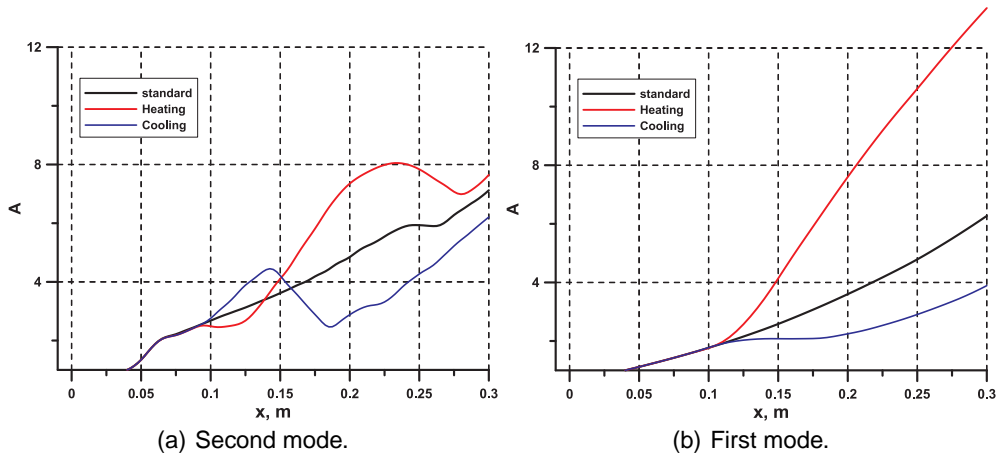


FIGURE 9. The distribution of the pulsation amplitudes along the plate.

the second mode. In the region of the heater the first mode growth rate significantly increased and reaches the level of the second mode. Downstream from the heater the first mode growth rate is still higher than for the base case. The analysis of an effect of wall temperature on the amplification rates revealed that stability of the second mode is not strongly affected for the temperature range studied. The principal effect in this case is connected with variation of the boundary-layer thickness. An effect of the wall temperature on the first mode stability is more important.

Figure 9(a) and Fig. 9(b) show the streamwise distributions of the maximum of the pulsations amplitude envelope calculated for wide range of frequencies for  $\chi = 0^\circ$  (second mode) and  $\chi = 55^\circ$  (first mode). In the reference case the pulsations of the first and second modes increase monotonically with increasing  $x$ . The level of the first mode pulsations is lower than corresponding value for the second mode. For the local cooling / heating test cases behavior of the second mode is qualitatively consistent with DNS results. Such a behavior is primarily associated with a shift of the frequency range of positive growth coefficients due to changes of  $\delta$ .

The distributions of the first mode pulsations amplitude are more monotonous. Local cooling and heating of the wall influence the first mode disturbance development along the entire zone. This is due to the fact that the temperature factor has a much greater effect on the first mode. Accordingly, the cooling / heating has a significant stabilization / destabilization effects on the first mode and effects associated with changes of  $\delta$  are less pronounced. The most interesting is the fact that as a result of the use of the heater level of the first mode begins to exceed the level of the second mode. At the same time the above shown data point out that the peak value of the amplification ratio of the second mode everywhere, except the heater, are higher than for the first mode. The growth rate peak of the first mode is much wider, therefore, the perturbations of the first mode have a longer distance for development. As a result the amplitude of the first mode fluctuations is higher than the amplitude of the second (in the case of the heater).

### 3. Three-dimensional simulations

This chapter deals with the influence of a three-dimensional heating/cooling element on the above described hypersonic flat-plate boundary layer. For the stability analysis of

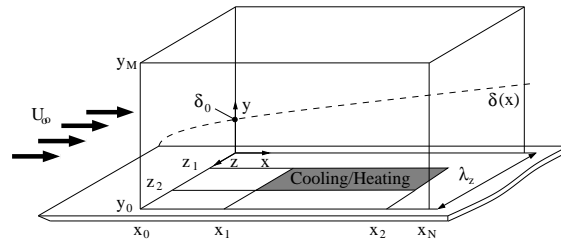


FIGURE 10. Integration domain.

the perturbed flow bi-global linear stability theory (BLST) is used, which provides two-dimensional eigenfunctions in spanwise crosscuts, e.g., in the wake of the perturbation element. The method has been already applied for the analysis of a discrete three-dimensional roughness element in a hypersonic boundary layer [6–9].

### 3.1. Steady Base Flow

#### 3.1.1. Governing Equations, Numerics and Discretization

A laminar hypersonic boundary-layer flow over a flat plate with a localized three-dimensional heating/cooling element is investigated. Figure 10 shows the rectangular integration domain. The steady primary state with the element is obtained by means of a time-accurate direct numerical simulation (DNS) with the in-house code NS3D. For more details concerning the numerical solver see [10]. The governing equations are non-dimensionalized with the reference length  $L = (\mu_{e,0} \cdot Re) / (\rho_{e,0} \cdot u_{e,0})$  and the values of velocity, density, temperature, viscosity and conductivity at the upper inflow boundary  $x_0 = 100 \text{ mm}$  (subscript  $e,0$ ). Note that the pressure is non-dimensionalized by  $(\rho_{e,0} u_{e,0}^2)$ . Air is treated as a non-reacting calorically perfect gas with constant Prandtl number  $Pr = 0.71$  and constant specific-heat ratio  $\kappa = c_p/c_v = 1.4$ . The Reynolds number  $Re$  are set to  $Re = 10^5$ . Sutherland's law is used to calculate the dynamic viscosity  $\mu$  as a function of temperature [11].

A self-similarity solution obtained from boundary-layer theory serves as initial flow field and provides the flow variables that are prescribed at the inflow ( $x = x_0 = 100 \text{ mm}$ ). The edge values of the Mach number, the temperature and the pressure at this position are taken from the 2-d simulations of Part I. Note that the weak shock emerging from the leading edge is not included. At the outflow ( $x = x_N = 350 \text{ mm}$ ), a buffer region is used, where all instantaneous flow variables are smoothly ramped to the initial condition. At the wall ( $y = y_0$ ), the no-slip, no-penetration boundary conditions are imposed on the velocity components. The pressure is calculated according to  $\partial p / \partial y|_w = 0$  and the density is computed from the equation of state. The wall is isothermal with  $T_w = 290 \text{ K}$ , and, with  $T_w/T_{rec} = 0.84$ , it is cooled. At the freestream boundary ( $y = y_M = 37.5 \text{ mm} \approx 12\delta_0$ ), all flow variables are computed such that the gradient along spatial characteristics is zero, except for the pressure, which is computed from the equation of state.  $\delta_0$  refers to the boundary-layer thickness at the inflow boundary  $x = x_0$ .

For the 3-d investigations the heating/cooling element is located at  $x_1 = 200 \text{ mm}$  downstream of the leading edge. Its streamwise and spanwise extent is set to  $|x_1 - x_2| = 50 \text{ mm} \approx 23\delta_0$  and  $|z_1 - z_2| = 25 \text{ mm} \approx 11.5\delta_0$ , respectively. For the cooled case the element has a temperature of  $T_C = 100 \text{ K}$  ( $T_C/T_w = 0.34$ ), whereas for the heated case a temperature of  $T_H = 440 \text{ K}$  ( $T_H/T_w = 1.52$ ) has been chosen. In order to smoothly connect the wall temperature with the temperature in the region of the element a 5<sup>th</sup>-order

Freestream Mach number $M_{e,0}$	5.27	[-]	
Freestream temperature $T_{e,0}$	1.00	[-]	61.075 <i>K</i>
Freestream pressure $p_{e,0}$	0.026	[-]	417.5 <i>pa</i>
Isothermal wall temperature $T_w$	4.75	[-]	290.0 <i>K</i>
Recovery temperature $T_{rec}$	5.68	[-]	346.9 <i>K</i>
Reference length $L$	1.00	[-]	21.37 <i>mm</i>
Periodicity length $\lambda_z$	3.1416	[-]	67.13 <i>mm</i>
Distance from the leading edge $x_1$	9.3589	[-]	200.0 <i>mm</i>
Streamwise element extent $ x_1 - x_2 $	2.3398	[-]	50.0 <i>mm</i>
Spanwise element extent $ z_1 - z_2 $	1.1699	[-]	25.0 <i>mm</i>
Element temperature $T_C/T_H$	1.64/7.20	[-]	100/440 <i>K</i>
$N_x \times N_y \times N_z$	1000 x 250 x 65	[points]	
$\Delta x$	$0.117 \cdot 10^{-1}$	[-]	
$\Delta y_0 - \Delta y_M$	$0.300 \cdot 10^{-2} - 2.412 \cdot 10^{-2}$	[-]	
$\Delta z$	$0.245 \cdot 10^{-1}$	[-]	
$\Delta t$	$0.314 \cdot 10^{-2}$	[-]	

TABLE 1. Simulation parameters.

polynomial is used, where both the gradient and curvature are zero at the beginning and at the end of the respective smoothing region. The temperature smoothing has a width of five millimeters in both streamwise and spanwise direction. 50000 time steps were computed in order to obtain a fully converged solution of the steady primary state. Table 1 contains an overview of the simulation setup.

### 3.1.2. Base-Flow Results

Figure 11 shows the wall-temperature distribution and the vortex visualization using constant values of  $\lambda_2$  [12] for the two investigated cases. Furthermore, spanwise cross-cuts of the temperature and  $u$ -velocity distribution at positions *A* and *C* are presented. In both cases it can be observed that the  $u$ -velocity is only slightly altered by the heating/cooling element leading to very weak vortical structures at the edges and in the near wake region of the element. Note that these structures are more pronounced for the cooled case, since the temperature ratio is higher than for the heated case. In contrast to the  $u$ -velocity distribution, the temperature field exhibits stronger gradients, which may lead to a different stability behavior of the flow. In order to determine the influence of the three-dimensionality of the heating/cooling element a bi-global linear stability analysis is performed. The red solid lines refer to the three positions, where the stability analysis is carried out. Note that two of these positions are located on the element (positions *A* and *B* at  $x = 212.5 \text{ mm}$  and  $x = 237.5 \text{ mm}$ , respectively) and one is positioned farther downstream at  $x = 262.5 \text{ mm}$  (position *C*).

## 3.2. Bi-global Linear Stability Theory

### 3.2.1. Governing Equations, Numerics and Discretization

Bi-global stability theory is applied for the stability analysis of the flow. Throughout this paper, the numerical scheme of Groskopf et. al. [6–9] is used. BLST is derived from the compressible three-dimensional Navier-Stokes equations, using a decomposition of all flow quantities into steady mean-flow terms and unsteady fluctuation terms. In addition to the well-known assumptions of primary linear stability theory the following holds for BLST: For the steady primary state a non-zero velocity component in wall-normal direc-

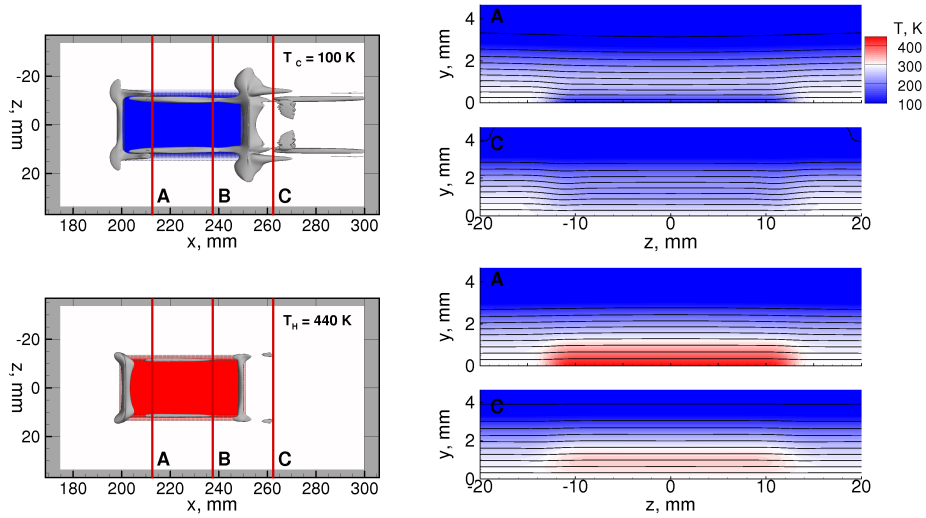


FIGURE 11. Left: Wall temperature distribution (color) and vortex visualization (shading, isosurfaces of  $\lambda_2 = -0.008$ ). Right: Spanwise crosscuts at positions *A* and *C* showing the temperature field and isolines of constant streamwise velocity ( $0.0\text{ m/s} < u < 826\text{ m/s}$ ,  $\Delta u = 82.6\text{ m/s}$ ).

tion is allowed, if it does not account for additional boundary-layer growth (i.e. the DC component is neglected). Furthermore, the complex amplitude distribution in the modal perturbation ansatz is two-dimensional. Note that the governing stability equations are treated in dimensionless form (see Sec. 3.1.1). Both mean flow and fluctuation terms are discretized on a structured mesh in the  $y$ - $z$  plane using compact finite differences of tenth order in spanwise direction and a spectral Chebyshev collocation method including a transformation for grid-point clustering in high-shear regions [13, 14] in wall-normal direction. The implicitly restarted Arnoldi method (see Arnoldi Package ARPACK [15]) is used to compute the resulting linear eigenvalue problem of the temporal approach. In order to determine spatial eigenvalues Gaster's relation is employed. For the eigenmode tracking a comparison of the eigenfunctions' amplitude shape (scalar product) is performed to identify the corresponding eigenvalues of the next tracking step.

### 3.2.2. Stability Results

First, the spatial amplification rates  $\alpha_{i,cg}$  of the most amplified eigenmode with zero spanwise wave number for the **2-d** element cases with and without heating/cooling element at position *A* are shown in Fig. 12.  $\alpha_{i,cg}$  is the growth obtained by Gaster's relation using the group velocity. The graph contains both the results obtained from NS3D/BLST (BLST used as standard LST: All variables are now invariant in  $z$ -direction) and the results of the commercial code FLUENT for the simulation of the primary state in combination with an in-house 2-d LST solver (LST<sub>Nov</sub>) for the stability analysis. It can be observed that the NS3D/BLST-tool kit leads to lower maximum amplification rates ( $\approx 15\%$  deviation). If LST<sub>Nov</sub> is used for the two baseflows (NS3D and FLUENT), the deviation is only less than five percent. (We note however that the BLST has been validated with an IAG in-house LST-solver, showing perfect agreement.) The frequency of the maximum amplification rates is in very good agreement. Note that the cooling also stabilizes the 2<sup>nd</sup> mode that has higher frequencies due to a local decrease of the boundary-layer

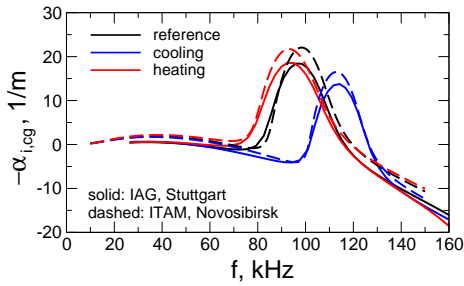


FIGURE 12. Spatial amplification rates vs. frequency for the 2d-cases and 2-d disturbances with and without thermal heating/cooling element at position  $A$ .

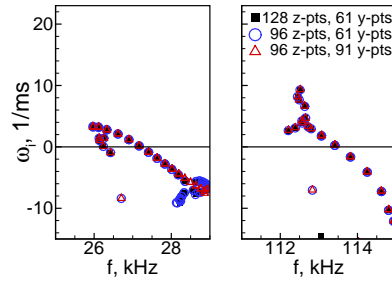


FIGURE 13. Eigenvalue spectra for the cooled 3-d case at position  $A$  obtained for  $\alpha_r = 106.8 \text{ mm}$  (left) and  $\alpha_r = 427.4 \text{ mm}$  (right).

thickness. The decrease must be caused by differing profiles  $u(y), T(y)$  compared to a self-similar boundary layer at the lower wall temperature.

Figure 13 shows the temporal amplification rate  $\omega_i$  as a function of the frequency  $\omega_r$  for the cooled 3-d element case at position  $A$ . The eigenvalue spectra are obtained for the streamwise wave numbers  $\alpha_r = 106.8 \text{ mm}$  and  $\alpha_r = 427.4 \text{ mm}$ , respectively, and contain the results for three different grid resolutions. Since the agreement for the physical modes is very good, grid independence is achieved using a resolution of 96 points in spanwise direction and 91 Chebyshev collocation points in wall-normal direction for all stability computations throughout this work.

The spatial amplification rates of the most amplified eigenmodes as a function of the frequency for the three investigated cases – cooled, heated and reference case – at the three different downstream positions are presented in Fig. 14. The figure contains the results for both the 2-d and 3-d heating/cooling element. It demonstrates that for all investigated cases (2-d or 3-d, heated or cooled) two-dimensional, high frequency  $2^{nd}$ -mode disturbances exhibit stronger growth rates and, thus, from a stability point of view, are more dangerous for the flow than obliquely traveling, low frequency  $1^{st}$ -mode disturbances. For the 2-d element cases it can be observed that heating results in higher  $1^{st}$ -mode amplification rates, whereas cooling has the opposite effect. Note further that above the temperature element cooling results in a frequency shift towards higher values for the most amplified  $2^{nd}$ -mode growth rates. Compared to the 2-d element case, the 3-d cooling results in slightly increased amplification rates at lower frequencies for both the  $1^{st}$ - and  $2^{nd}$ -mode disturbances. Again, the 3-d heating has the opposite effect. Note that no increase of  $1^{st}$ -mode amplification rates is observed for the 3-d cases. It can be stated that despite the three-dimensionality of the heating/cooling element  $1^{st}$ -mode disturbances play a minor role for the investigated setup. Note further that for the position downstream of the temperature element the  $2^{nd}$ -mode disturbances show a similar behavior for all investigated cases. The effects of the thermal perturbation element seem to be restricted to its streamwise extent.

Figure 15 illustrates the  $T'$ -eigenfunction distribution corresponding to the most amplified  $1^{st}$ -mode disturbances (see Fig. 14) at the three investigated  $y$ - $z$ -planes for the cooled and heated case. Additionally, the graph contains the temperature distribution of the steady base flow solution. For comparison, the  $1^{st}$ -mode  $T'$ -eigenfunction distribution corresponding to the most amplified growth rates for the 2-d heating and cooling at position  $A$  (Fig. 15 top) is also included. Note that the eigenfunction distribution of the

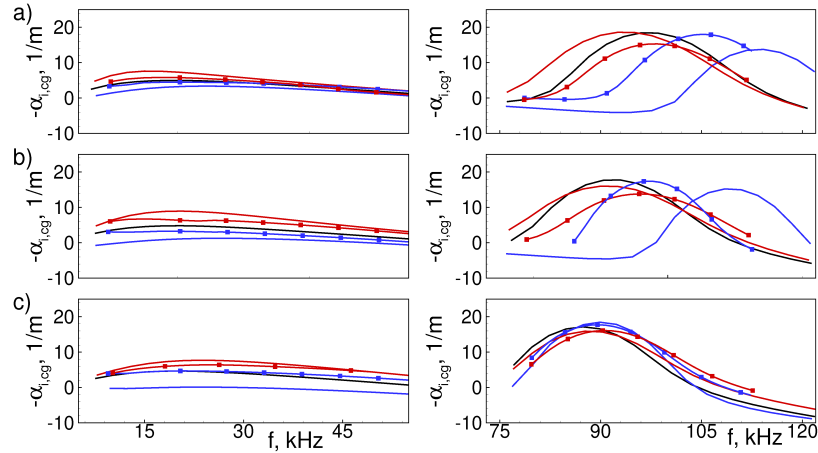


FIGURE 14. Spatial amplification rate vs. frequency for the cases with and without heating/cooling element at positions *A-C* (a-c)). Left:  $1^{st}$ -mode. Right:  $2^{nd}$ -mode. Symbols refer to the 3-d cases, whereas solid lines without symbols label the 2-d cases (propagation angle of the 2-d waves:  $\chi = 0$ ). Black stands for the reference case, blue for the cooled case and red for the heated case.

2-d element cases is similar for all three locations. Hence, only position *A* is presented. The thick solid line at  $y = 0$  mm refers to the spanwise extent of the heating/cooling element. For the 2-d element cases a pearl-necklace-like structure of the  $T'$ -eigenfunction distribution can be observed, representing the  $\pm$  obliquely traveling disturbance waves as a standing wave in spanwise direction. The distortion of the 3-d  $T'$ -eigenfunctions is rather weak for position *A*. For heating, the structures are similar in shape and extent as for the 2-d element case, whereas for cooling significant differences appear. The average spanwise wavelength is now given by the cooling element width. Further downstream this effect relaxes. It is worth noting that the  $1^{st}$ -mode  $u'$ -eigenfunctions, which exemplarily are plotted in Fig. 16 for position *A*, show a similar behavior. It can be observed that the  $u'$ -distribution merely differs from the  $T'$ -eigenfunction, although the gradients of the temperature field are much stronger than the gradients of the  $u$ -velocity (see Fig. 11).

The  $T'$ -eigenfunction distribution of the  $2^{nd}$ -mode disturbances (corresponding to the most amplified growth rate of Fig. 14) is displayed in Fig. 17. The graph shows the results for the heated and cooled case at the three investigated positions. For comparison, the left column illustrates the eigenfunctions of the 2-d element cases with and without heating/cooling element. Since they are two-dimensional and not varying in spanwise direction, these eigenfunctions are plotted as function of  $y$  only. The  $T'$ -eigenfunctions of the 3-d element cases are found to be locally isolated and strongly distorted in spanwise direction, where the maximum is either sitting on top of the thermal element or in between two elements. Note that for the heated case the same mode (locally isolated over the element and symmetric) seems to be dominant at all positions *A-C*. For the cooled case, however, the most dominant mode varies from locally isolated and symmetric at position *A* to locally isolated and anti-symmetric at position *B*. Finally, at position *C* the most dominant mode resembles the 2-d element case except for the wake region of the element. Hence, the three-dimensional character of the eigenfunctions for both the heated and cooled case is still present for position *C* downstream of the element. This is in contrast to the findings of Fig. 14, where the growth rates exhibit no major difference

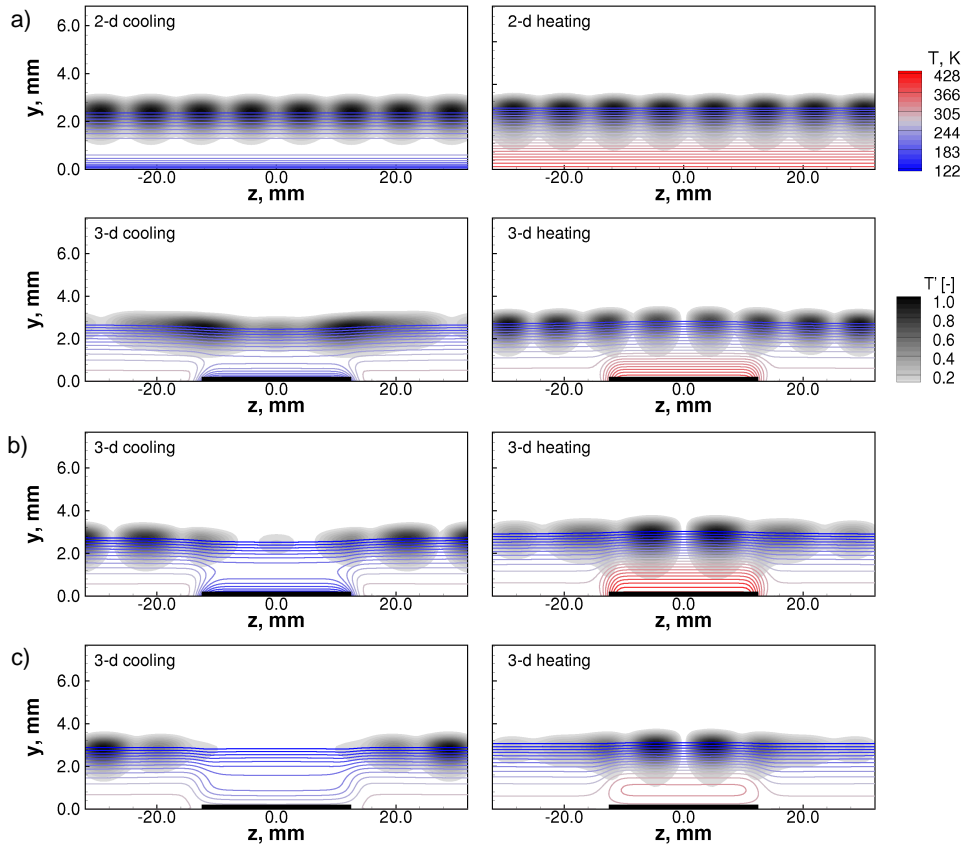


FIGURE 15.  $1^{st}$ -mode  $T'$ -eigenfunction and temperature distribution of the primary state in spanwise crosscuts at positions A-C (a-c) for the cooled (left) and heated (right) 3-d case. The eigenfunctions of the 3-d cases correspond to the respective most amplified frequency of Fig. 14-left. For comparison, the 2-d heating and cooling at position A is also included (top), now showing a 3-d disturbance wave at propagation angle  $\chi \approx 58^\circ$  (contradictory to Fig. 14-left). Isocontours refer to the modulus of the perturbation amplitude  $T' = |\hat{T}|$  normalized by the maximum of  $T'$ , solid lines indicate the temperature distribution of the primary state. Axis not to scale.

between the 2-d and 3-d element case. Similar to the first mode the  $u'$ -eigenfunctions of the second mode do not differ qualitatively from the  $T'$ -eigenfunction distribution either (not shown).

The N-factor curves ( $N = -\int_x \alpha_{i,cg} dx$ ) for the integrally most amplified frequency ( $f = 87.7 kHz$ , a second mode in the reference case) of the 2-d and 3-d cases gained by the NS3D/BLST-package are shown in Fig. 18. Compared to the reference case, the **heated** 2-d element case exhibits a slight increase of the N-factor in the region of the element. Downstream of the element, however, the N-factor has the same slope as the reference curve. In compliance with Fig. 14 the N-factor of the 3-d heating is growing slower as the 2-d case in the region of the element (now a 3-d second mode), but exhibits the same slope as the reference and 2-d heated case farther downstream. For the **cooled** 2-d element case the N-factor is decreasing at first due to a shift of the amplified second modes to higher frequencies ( $\delta^*$  is locally decreased), and thus the fixed frequency is now rather in the region between the second and first mode instability

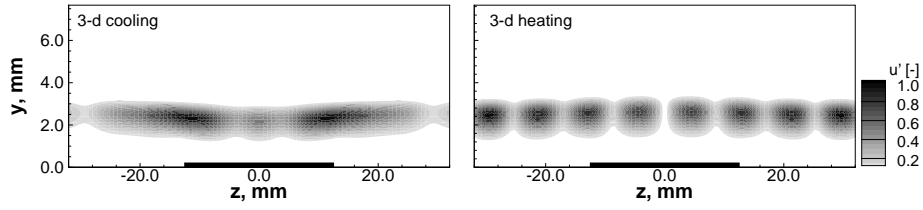


FIGURE 16. 1<sup>st</sup>-mode  $u'$ -eigenfunction distribution in a spanwise crosscut at position  $A$  for the cooled (left) and heated (right) case. Isocontours refer to the modulus of the perturbation amplitude  $u' = |\hat{u}|$  normalized by the maximum of  $u'$ . Axis not to scale.

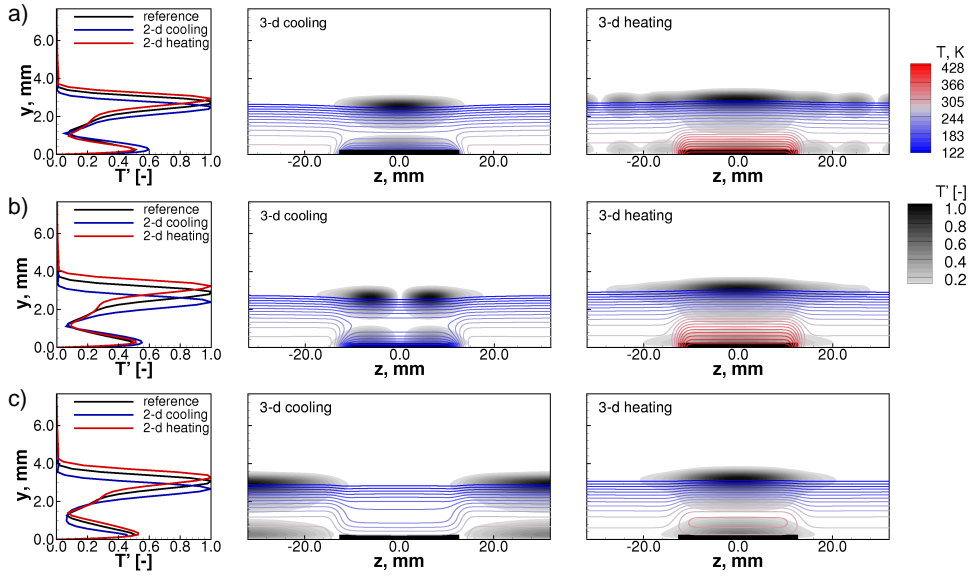


FIGURE 17. 2<sup>nd</sup>-mode  $T'$ -eigenfunction and temperature distribution of the primary state in spanwise crosscuts at positions  $A$ - $C$  (a-c)) for the cooled (middle column) and heated (right column) case. The eigenfunctions correspond to the respective most amplified frequency of Fig. 14-right. For comparison, the 2<sup>nd</sup>-mode  $T'$ -eigenfunctions of the 2-d cases are also included (left column). Isocontours refer to the modulus of the perturbation amplitude  $T' = |\hat{T}|$  normalized by the maximum of  $T'$ , solid lines indicate the temperature distribution of the primary state. Axis not to scale.

for 2-d waves (note that 2-d first mode waves are hardly amplified). The changeover from second to first mode has been verified by looking at the wall-normal phase profiles of the pressure disturbances (first mode disturbances show virtually constant phase, second mode disturbances exhibit a phase jump near the wall). Downstream the N-factor grows at the same slope as the reference curve behind the element, because the 2-d second mode is nearly regained. In contrast to that, the cooled 3-d element case (based on the downstream development of the most dominant 2<sup>nd</sup> mode at position  $A$ ) shows an almost neutrally behavior on the cooling element, because the disturbance is now nearly a 3-d first mode that is more amplified than a 2-d first mode, before it increases in the region of the trailing edge. Farther downstream the recovery of the 3-d second mode takes longer, visible by the still reduced growth. Apparently, the effect of the thermal element is approximately limited to its streamwise extent and leads to a shift of the N-factor development, here for the 2-d cooling element to  $\Delta N = -0.56$ .

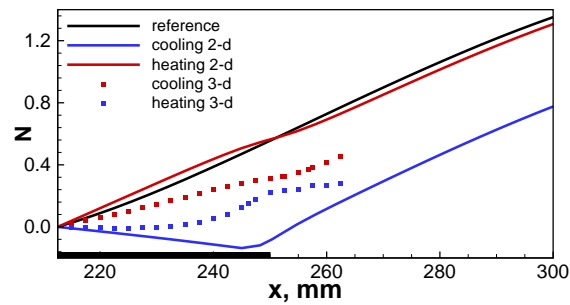


FIGURE 18. N-factor curves of all investigated cases for the integrally most amplified frequency ( $f = 87.7 kHz$ , solid curves represent 2-d modes, for the reference case it is a second mode). The thick solid line marks the streamwise extent of the heating/cooling element.

#### 4. Conclusions

At first, the development of the disturbances in a hypersonic boundary layer with a two-dimensional local heating and cooling element at the wall was studied using DNS and LST. It was shown that both approaches deliver similar results for the investigated 2-d disturbances. The results of the simulations show that the variation of the boundary-layer thickness due to the local temperature variation has a significant effect on the development of the second mode disturbances. At the same time the wall temperature strongly affects the stability of the first mode which may dominate the transition in the case of local wall heating. Based on the analysis of the numerical simulation, it can be concluded that the local heating of the wall results in an increase of pulsations everywhere, except for the region of the heater. The cooler may be used for transition delay, but it has to be done carefully in order to prevent a premature transition on it. The effect of the local amplification above the cooler is more pronounced if the boundary-layer thickness is significant. Taking into account that the local amplification on the cooler is much higher if it is placed far downstream, it has to be located close to the model leading edge.

In addition, the influence of a three-dimensional heating/cooling element was investigated. The stability behavior of the flow regime was analyzed by means of the bi-global linear stability theory at three different  $y$ - $z$  cross-planes and compared with the results of the corresponding two-dimensional cases. It was shown that despite the three-dimensionality of the heating/cooling element  $1^{st}$ -mode disturbances play a minor role. The 3-d effects are found to be rather weak and seem to be restricted to the region of the element. As the unperturbed flat-plate behavior is likely to be restored in the wake of the element (as the results found here so far suggest), the N-factor shift caused by the element defines the promotion or delay of transition. Only a delay has been found by local cooling despite the  $2^{nd}$  mode is primarily affected. While the tracking of rms-amplitudes cannot clarify the role of the dominating frequencies, the N-factor curves gained using distinct frequencies allow the scrutinization of the prevailing mechanisms. Locally, a fixed-frequency mode is pushed from the  $2^{nd}$ -mode to the  $1^{st}$ -mode region due to the decreased boundary-layer thickness. Thus, a drop-off in growth results, causing a reduced integral amplification of second mode disturbances along the plate.

## Acknowledgments

The financial support of the German Research Foundation (Deutsche Forschungsgemeinschaft – DFG) in the framework of the Sonderforschungsbereich/Transregio 40 and the computational resources, kindly provided by the Federal High Performance Computing Center Stuttgart (HLRS), are gratefully acknowledged. Special thanks go to the organizing committee of the summer research program.

## References

- [1] SOUDAKOV, V. G., EGOROV, I. V. AND FEDOROV, A. V. (2009). Numerical simulation of receptivity of a hypersonic boundary layer over a surface with temperature jump. *Proceedings of the 6th European Symposium on Aerothermodynamics for Space Vehicles*, Versailles, France, November 3-6, 2008.
- [2] MACK L. M. (1969). Boundary-layer stability theory. *Internal document no. 900-277, Rev. A.*, JPL, Pasadena, CA, USA.
- [3] MACK L. M. (1989). On the inviscid acoustic-mode instability of supersonic shear flows. *Theoret. Comput. Fluid Dynamics*, **2**, 97–123.
- [4] MA, Y. AND ZHONG, X. (2003). Receptivity of a supersonic boundary layer over a flat plate. Part 1. Wave structures and interactions. *J. Fluid Mech.*, **488**, 31–78. doi:10.1017/S0022112003004786.
- [5] MA, Y. AND ZHONG, X. (2003). Receptivity of a supersonic boundary layer over a flat plate. Part 2. Receptivity to free-stream sound. *J. Fluid Mech.*, **488**, 79–121. doi:10.1017/S0022112003004798.
- [6] GROSKOPF, G., KLOKER, M. J. AND MARXEN, O. (2008). Bi-global secondary stability theory for high-speed boundary-layer flows. In: *Proceedings of the CTR Summer Program 2008*, 55–72.
- [7] GROSKOPF, G., KLOKER, M. J. AND MARXEN, O. (2009). Bi-global crossplane stability analysis of high-speed boundary-layer flows with discrete roughness. In: *Proceedings of the 7th IUTAM Symposium on Laminar-Turbulent Transition*, Stockholm, Sweden, June 23-26, 2009.
- [8] GROSKOPF, G., KLOKER, M. J., STEPHANI, K. A., MARXEN, O. AND IACCARINO, G. (2010). Hypersonic flows with discrete oblique surface roughness and their stability properties. In: *Proceedings of the CTR Summer Program 2010*, 405–422.
- [9] GROSKOPF, G., KLOKER, M. J. AND STEPHANI, K. A. (2011). Temperature/rarefaction effects in hypersonic boundary-layer flow with an oblique roughness element. *41st AIAA Fluid Dynamics Conference and Exhibit, AIAA 2011-3251*, Honolulu, HI, USA, June 27-30, 2011.
- [10] BABUCKE, A., LINN, J., KLOKER, M. J. AND RIST, U. (2006). Direct numerical simulation of shear flow phenomena on parallel vector computers. In: Resch, M. et al. (Eds.), *High Performance Computing on Vector Systems*. High Performance Computing Center, Stuttgart (HLRS), 229–247. Springer.
- [11] WHITE, F. M. (1991). *Viscous Fluid Flow*. McGraw-Hill.
- [12] JOENG, J. AND HUSSIAN, F. (1995). On the identification of a vortex. *J. Fluid Mech.*, **285**, 69–94. doi:10.1017/S0022112095000462.
- [13] ERLEBACHER, G. AND HUSSAINI, M. Y. (1991). Nonlinear evolution of a second-mode wave in supersonic boundary layers. *Applied Numerical Mathematics*, **7**, 73–91. doi:10.1016/0168-9274(91)90104-8.

- [14] KOCH, W., BERTOLOTTI, F. P., STOLTE, A. AND HEIN, S. (2000). Nonlinear equilibrium solutions in a three-dimensional boundary layer and their instability. *J. Fluid Mech.*, **406**, 131–174.
- [15] LEHOUCQ, R. B., SORENSEN, D. C. AND YANG, C. (1998). *ARPACK User's Guide*, SIAM, Philadelphia, PA, USA.